

Comparison of densification and distortion behaviors of W-Ni-Cu and W-Ni-Fe heavy alloys in liquid-phase sintering

YUNXIN WU, R. M. GERMAN, B. MARX, P. SURI, R. BOLLINA
Center for Innovative Sintered Products, P/M Lab, 147 Research West Building,
The Pennsylvania State University, University Park, PA 16802-6809, USA
E-mail: rmg4@psu.edu

This paper aims to correlate the densification and distortion behaviors of liquid-phase sintered 80W-14Ni-6Cu and 80W-14Ni-6Fe heavy alloys with the melting characteristics of the Ni-Cu and Ni-Fe matrices. Differential thermal analysis (DTA) of die-pressed compacts reveals that the melting range of the Ni-Cu matrix is extended from 1235°C to 1453°C by the *in situ* alloying between elemental Cu and Ni powders, whereas the melting of the Ni-Fe matrix is limited to a narrow temperature range between 1464°C and 1480°C. Dilatometry and furnace sintering tests show that densification due to liquid-phase sintering of 80W-14Ni-6Cu starts at 1287°C and proceeds at a low rate to 1450°C, where full densification without distortion is achieved. In contrast, densification due to liquid-phase sintering of 80W-14Ni-6Fe occurs at a very high rate above 1475°C, and full density can be obtained at 1500°C. For both alloy compacts, distortion is induced by prolonging the sintering time or elevating the sintering temperature after full densification. Crack-like voids develop in the 80W-14Ni-6Cu compact to accommodate the gravity-induced distortion, while spherical pores are dominantly formed in the 80W-14Ni-6Fe compact as a result of water vapor entrapment. © 2003 Kluwer Academic Publishers

1. Introduction

Tungsten heavy alloys (WHAs) are two-phase composites with tungsten grains dispersed in an alloy matrix. The combination of density, ductility, strength, thermal conductivity, and corrosion resistance makes them unique in many applications, such as radiation shields, vibration dampers, kinetic energy penetrators, and heavy-duty electrical contacts. The WHAs are usually fabricated by liquid-phase sintering (LPS) from W-Ni-Fe or W-Ni-Cu elemental powder mixes [1–3]. During LPS, the nickel-alloy melt, which has a high solubility for tungsten, dissolves the tungsten-tungsten bonds that are formed during solid-state sintering [4–6]. When the solid bonds are penetrated, particle rearrangement and pore filling occur, resulting in rapid densification of the compact. The subsequent solution-precipitation process also depends on tungsten solubility and contributes to tungsten grain shape accommodation, which gives better solid packing and releases additional liquid to fill any remaining inter-grain pores [7].

However, the liquid-phase sintered WHAs are susceptible to distortion and slumping, because the attributes that allow rapid densification also contribute to weakening of the compact during sintering [8]. Penetration of solid bonds by newly formed nickel melt leads to a substantial loss of compact strength. In addition, the capillary contracting force provided by the

liquid decays as the void space between tungsten grains becomes saturated with liquid. Upon approaching full density with concomitant loss of capillary forces, if no new solid-solid bonds exist, then the structure distorts by viscous flow in response to gravitational force [9, 10]. The large density difference (over 10000 kg/m³) between tungsten and liquid matrix enhances distortion and slumping by inducing severe solid settling and solid-liquid segregation [11–13]. Therefore, full densification and shape retention are two main concerns for LPS of WHAs.

To maintain structural rigidity during LPS, the liquid volume needs to be restricted. It was found that a connected solid structure that resists distortion could be attained when the liquid volume is less than 20% [9, 10, 14]. Accordingly, most of the earlier works on LPS of WHAs used high tungsten contents in the range 88 to 98 wt% [2, 3, 7, 15–19]. However, a high tungsten content leads to not only a slow densification in sintering, but also a drastic reduction in ductility due to high sensitivity of intergranular failure [15, 16]. In comparison, a medium tungsten content (e.g., 80 wt%) facilitates fast densification, and produces rounded tungsten grains with low W-W contiguity in the LPS microstructure, which aid in improving mechanical properties [14]. Therefore, recent efforts have been devoted to understanding the distortion behavior of the WHAs that have tungsten contents of about 80 wt% [20–27]. These

works showed that shape retention could be achieved by manipulating the green microstructural parameters and controlling the sintering conditions. Nevertheless, the evolution processes of densification, distortion, and microstructure have not been fully understood. In particular, since the liquid phase governs the densification and distortion kinetics, the effects of Ni-Cu and Ni-Fe liquid-phase formation needs to be further characterized for the two typical WHA systems: W-Ni-Cu and W-Ni-Fe.

The present work aims to correlate the densification and distortion behaviors of 80W-14Ni-6Cu and 80W-14Ni-6Fe compacts with the characteristics of Ni-Cu and Ni-Fe liquid-phase formation. Differential thermal analysis (DTA) was performed to trace the melting processes of the alloy matrices. Dilatometry and furnace sintering tests were carried out to examine the evolutions of sintering shrinkage, densification, and distortion. In combination with microstructural analysis, the contributions of Ni-Cu and Ni-Fe liquid matrices to LPS of WHAs were investigated qualitatively.

2. Experimental procedures

The tungsten heavy alloys investigated in this work were 80W-14Ni-6Cu (65.2W-24.3Ni-10.5Cu) and 80W-14Ni-6Fe (64.3W-24.0Ni-11.7Fe) with the compositions given in weight percent and corresponding volume fractions given in parentheses. The Ni:Cu and Ni:Fe ratios were maintained at 7:3, which was considered optimal to avoid deleterious intermetallic phases in W-Ni-Fe alloy systems [28]. Both alloys were fabricated from mixed elemental powders, the characteristics of which are summarized in Table I. The as-received tungsten powder was first deagglomerated by rod milling for 1 h in a polyethylene jar back-filled with argon, then mixed with either nickel and copper or nickel and iron powders. To help control the green porosity and pore size, a clean-burning polymer, ethylene-*bis*-stearamide (EBS) [24, 25], was added to the powder mixtures. The mean particle size of the EBS polymer was 36 μm . After mixing the elemental powders in a Turbala mixer for 20 min to achieve homogeneity, the powder mixtures were weighed and uniaxially die pressed at 175 MPa into cylinders 12.8 mm in diameter and 10.0 mm in height. The EBS polymer in the cylindrical compacts was thermally debound by heating the compacts to 550°C at 5°C/min and holding at 550°C for 1 h in dry hydrogen. The resulting green

porosities of the compacts were measured as 57% for 80W-14Ni-6Cu, and 55% for 80W-14Ni-6Fe.

Differential thermal analysis (DTA) was performed for both alloy systems using a Simultaneous DTA-TGA Instrument (TA Instruments) in argon. The samples were cut from the debound cylindrical compacts, with a weight less than 0.15 g. The thermal cycle for DTA test is as follows: heating to 1490°C at 10°C/min with an intermediate 1 h hold at 900°C, holding at 1490°C for 5 min, followed by cooling at 10°C/min. The temperature difference between the sample and the high-purity alumina reference was recorded to trace the endothermic and exothermic peaks during the thermal cycle. Dilatometry was carried out using an Anter vertical pushrod dilatometer in a dry hydrogen atmosphere (dew point -36°C). The cylindrical compacts of both alloy systems were subject to the same thermal cycle as that used in the DTA test. The *in situ* sintering shrinkage and shrinkage rate were plotted against temperature.

Furnace sintering was performed in a CM horizontal tube furnace in dry hydrogen (dew point -36°C) with the same thermal cycle as that used in the DTA and dilatometry tests. The 1 h hold at 900°C was primarily used to reduce the surface oxides on the powders [15, 25]. The peak sintering temperature ranged from 1275°C to 1500°C, and the holding time was 1 min. In order to investigate the time-dependent sintering behavior after liquid-phase formation, a 30 min hold was additionally applied to the sintering above 1400°C. After sintering, the compact shapes were examined macroscopically for distortion evaluation, and then the densities were measured using the Archimede's method. Finally, the samples were sectioned along the longitudinal direction, mounted, and polished to a submicron finish. The unetched microstructures were observed under optical microscope.

3. Results and discussion

3.1. Differential thermal analysis (DTA)

The DTA curves of the 80W-14Ni-6Cu and 80W-14Ni-6Fe compacts are shown in Fig. 1. For the 80W-14Ni-6Cu compact, neither endothermic nor exothermic peak can be found around the melting point of elemental copper, 1083°C; instead, three sequential endothermic peaks (A, B, and C) are formed between 1235°C and 1453°C during heating, and the corresponding exothermic peak (D) upon cooling is extended from 1434°C to 1251°C, which can be considered as the equilibrium

TABLE I Characteristics of W, Ni, Cu and Fe powders

Powder	W	Ni	Cu	Fe
Vendor	Osram Sylvania	Novamet	ACuPowder	ISP
Grade	M-37	123	635	CIP-R-1470
D_{10} (μm)	1.8	4.7	7.9	2.3
D_{50} (μm)	4.8	10.8	12.1	5.9
D_{90} (μm)	9.3	25.7	18.9	14.8
Pycnometer density (g/cm^3)	19.1	8.9	8.8	7.9
Apparent density (g/cm^3)	3.7	2.3	3.3	2.1
Tap density (g/cm^3)	6.1	3.3	3.9	3.6
Melting Point ($^\circ\text{C}$)	3410	1453	1083	1535

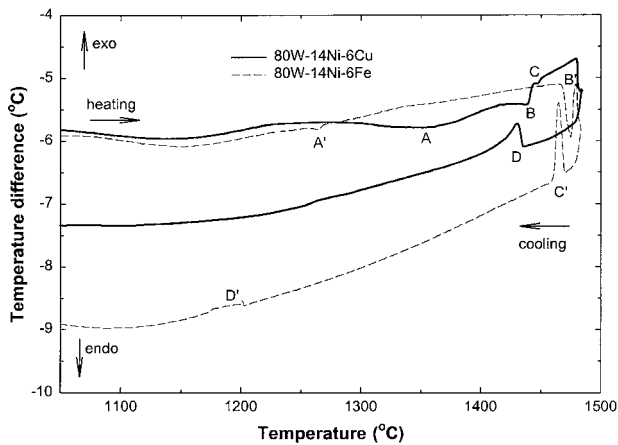


Figure 1 Results of differential thermal analysis (DTA) for 80W-14Ni-6Cu and 80W-14Ni-6Fe compacts.

liquidus and solidus temperatures respectively. According to the Cu-Ni and Cu-W phase diagrams [29], copper has complete, mutual solubility for nickel but practically no solubility for tungsten, and the Cu-Ni alloys have intermediate solidus temperatures between the Cu and Ni melting points. The earlier results of X-ray diffraction analysis by Heckel *et al.* [30] revealed that significant homogenization in the Ni (52 at.%)–Cu compact could result from the Ni-Cu inter-diffusion after 1 h sintering at 950°C, but complete homogenization would require a 60 h hold at this temperature. In this work, the Cu:Ni ratio in the 80W-14Ni-6Cu compact is much lower. Hence it may be suggested that the copper powders in the 80W-14Ni-6Cu compact forms a solid solution with nickel via elemental inter-diffusion prior to copper melting. Moreover, due to the insufficient diffusion time in the non-equilibrium sintering process and the resulting local variation in the composition of the Ni-Cu solid solution, the equilibrium melting behaviors dictated by the Ni-Cu phase diagram, with a solidus and liquidus temperatures of 1387°C and 1406°C respectively, cannot be expected here with the *in situ* alloyed Ni-Cu matrix; instead, the Ni-Cu liquid phase forms over a wide temperature range below the melting point of elemental nickel.

Compared with 80W-14Ni-6Cu, the 80W-14Ni-6Fe compact exhibits a much narrower temperature range for liquid-phase formation and solidification. During heating, the endothermic peak (B') that represents the melting of the Ni-Fe matrix is formed between 1464°C and 1480°C. In accordance, the exothermic peak (C') for liquid-phase solidification appears between 1469°C and 1459°C, which can be considered as the equilibrium liquidus and solidus temperatures respectively. It is evident that the melting temperature of the Ni-Fe matrix is well above the melting point of elemental nickel and does not significantly change with the *in situ* alloying among elemental Ni, Fe, and W powders. This result agrees with the equilibrium Fe-Ni and Fe-Ni-W phase diagrams. According to the Fe-Ni phase diagram [31], iron and nickel are mutually soluble over a wide temperature range. The 30:70 (γ Fe, Ni) alloy melts congruently at 1445°C. In the Fe-Ni-W ternary alloy phase diagrams [32], (γ Fe, Ni) also acts as one of the

main phases between 800°C and 1500°C, and the eutectic Ni-Fe-W liquid phase forms at 1465°C. Besides liquid-phase formation, the sintering process in the W-Ni-Fe alloy system may also involve some other phase changes, most of which relate to the formation of intermetallics [33]. As evident in Fig. 1, an endothermic peak (A') forms at 1257–1273°C for the 80W-14Ni-6Fe compact during heating, and an exothermic peak (D') appears at 1201–1172°C upon its cooling. These two peaks are very likely resulted from the transformation of Fe₇W₆, which is the sole intermetallic phase in the Fe-Ni-W alloy system above 1150°C [32], as well as in the Fe-W alloy system above 1190°C [34].

3.2. Dilatometry

Fig. 2 plots the dilatometric data of sintering shrinkage and shrinkage rate versus temperature for the 80W-14Ni-6Cu and 80W-14Ni-6Fe compacts. As shown, the 80W-14Ni-6Cu compact swells slightly between 650°C and 900°C. According to our previous investigation [35], the swelling is related to the expansion of water vapor, which is produced by the reaction between hydrogen atmosphere and the oxygen impurities of copper powder. Since the iron powder is produced by carbonyl process, it contains much less oxygen (around 300 ppm [23]) than the water-atomized copper powder (about

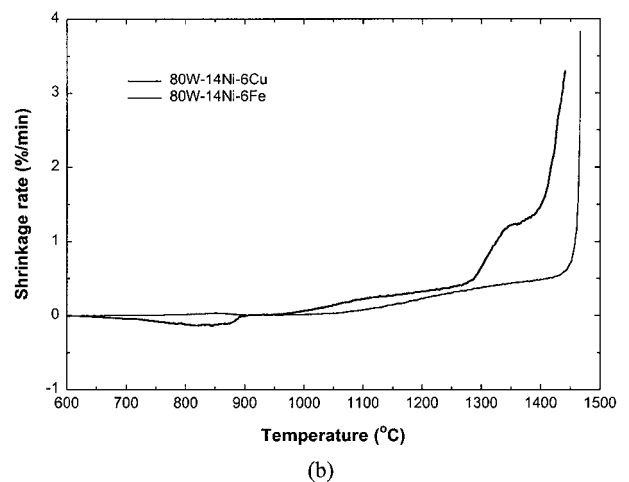
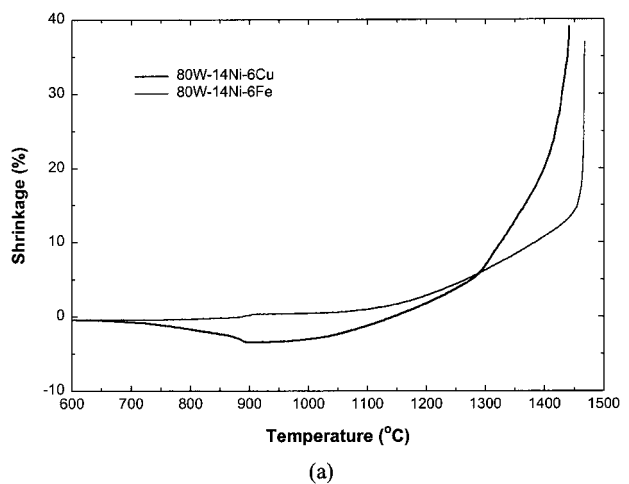


Figure 2 Dilatometry curves of (a) shrinkage and (b) shrinkage rate versus temperature for 80W-14Ni-6Cu and 80W-14Ni-6Fe compacts.

1800 ppm [35]). Therefore, no substantial swelling occurs to the 80W-14Ni-6Fe compact. The 1 h hold at 900°C completes the reducing reaction and removes the water vapor from the 80W-14Ni-6Cu compact. As heating continues, solid-state sintering starts above 950°C on both compacts, and their shrinkage and shrinkage rate increase progressively with temperature. Note that the shrinkage rates of both compacts are very comparable during the solid-state sintering, primarily owing to their similarity in green density and identity in compositional ratio.

When the temperature rises over 1287°C, however, the 80W-14Ni-6Cu compact shows a rapid increase in shrinkage rate, whereas the 80W-14Ni-6Fe compact maintains its slow shrinkage rate until 1460°C. This is consistent with the DTA results and signifies the earlier onset of liquid-phase sintering in the 80W-14Ni-6Cu compact. By comparing the shrinkage rates upon liquid-phase sintering, it can be found that liquid-phase sintering proceeds mildly in 80W-14Ni-6Cu, but dramatically in 80W-14Ni-6Fe. This difference reflects on the distinct characteristics of the Ni-Cu and Ni-Fe liquid-phase formation. As the *in situ* alloyed Ni-Cu matrix melts over a wide temperature range, a gradual increase in nickel concentration is expected for the Ni-Cu liquid phase. According to the works of Ermenko *et al.* [36] and Johnson *et al.* [19], the solubility of tungsten in the Ni-contained melt increases with the nickel concentration. Therefore, liquid-phase sintering of the 80W-14Ni-6Cu compact is facilitated gradually with the melting of the Ni-Cu matrix, and an obvious incubation period exists between the beginning of Ni-Cu liquid-phase formation (1235°C) and the start of liquid-phase sintering (1287°C). During the incubation period, the liquid-phase volume accumulates so as to initiate the liquid-phase sintering process [9, 37]. On the contrary, the melting of the Ni-Fe matrix in the 80W-14Ni-6Fe compact occurs within a narrow temperature range above the nickel melting point. As a result, fast dissolution of W-W bonds is facilitated by the intensively increased content of the Ni-Fe-W eutectic liquid phase, thus leading to a rapid densification of the compact.

3.3. Sintered density

Although dilatometry provides *in situ* measurement of the sintering events, an additional influence on the liquid-phase sintering might result from the external pressure exerted by the dilatometer pushrod on the top surface of the dilatometry sample. This pressure is estimated as 0.05 MPa, very comparable to the compact strength when a high volume liquid phase is present [9]. Therefore, examinations on the furnace-sintered samples can help understand the densification and distortion processes of the WHAs from a more practical standpoint.

Fig. 3 plots the relative densities of the 80W-14Ni-6Cu and 80W-14Ni-6Fe compacts sintered at different temperatures. It can be seen that the densification processes of the two compacts agree with their respective dilatometry behavior. Solid-state sintering to 1275°C produces only a 53% dense 80W-14Ni-6Cu and a 55%

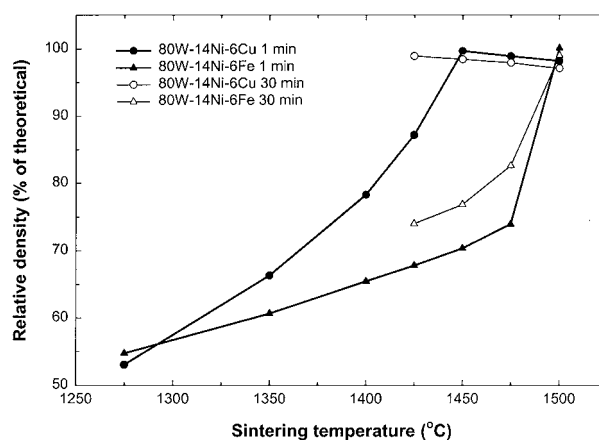


Figure 3 Sintered densities of 80W-14Ni-6Cu and 80W-14Ni-6Fe compacts as a function of sintering temperature.


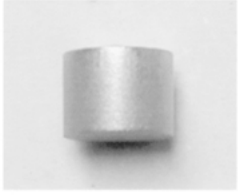
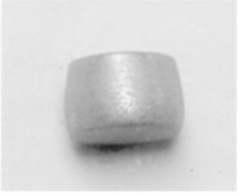






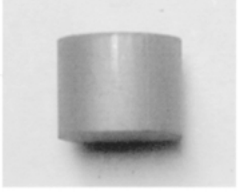
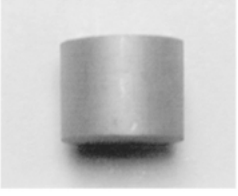
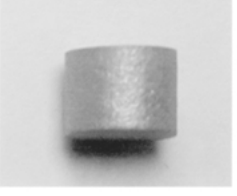

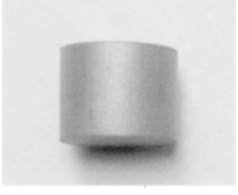
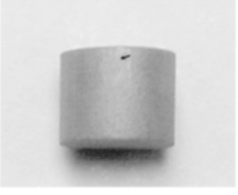

dense 80W-14Ni-6Fe. Note that the green densities of these two compacts are 43% and 45% of theoretical, respectively. When liquid-phase sintering starts above 1287°C in the 80W-14Ni-6Cu compact, a large difference in density appears between 80W-14Ni-6Cu and 80W-14Ni-6Fe. The 80W-14Ni-6Cu compact exhibits an increasing densification rate with temperature, and full density is obtained at 1450°C. In contrast, the 80W-14Ni-6Fe compact maintains a much lower densification rate at this stage, and achieves only 74% density when sintered to 1475°C, due to the absence of liquid phase. However, dramatic increase in the densification rate is induced above 1475°C by the Ni-Fe liquid-phase sintering, and full densification can be rapidly obtained when sintered to 1500°C.

Fig. 3 also shows that the fully densified compacts are subject to density degradation with prolonged sintering time or higher sintering temperature. For instance, the relative density of the 80W-14Ni-6Cu compact decreases from 100% at 1450°C for 1 min to 98.4% at 1450°C for 30 min, and to 98.8% at 1475°C for 1 min. Similarly, the relative density of the 80W-14Ni-6Fe compact is reduced from 100% at 1500°C for 1 min to 98.9% at 1500°C for 30 min. The reasons involved will be analyzed below in association with the distortion and microstructural changes of the compacts.

3.4. Distortion

The photographs of the furnace-sintered compacts are shown in Table II for qualitative evaluation of shape distortion. It is evident that the fully densified 80W-14Ni-6Cu compact does not distort when sintered at 1450°C for 1 min. However, significant distortion occurs by prolonging the holding time at 1450°C to 30 min, or elevating the sintering temperature to 1475°C. Likewise, the 80W-14Ni-6Fe compact retains its shape until full densification is achieved at 1500°C, and severe distortion occurs when a prolonged hold of 30 min at this temperature is applied. These results provide further evidence that densification and distortion are sequential events during LPS: densification occurs first, and then distortion takes place as a result of the loss of structural rigidity of the compact [9, 10, 24, 25]. The

TABLE II Photographs of sintered 80W-14Ni-6Cu and 80W-14Ni-6Fe compacts

Materials and sintering time	Sintering temperature			
	1425°C	1450°C	1475°C	1500°C
80W-14Ni-6Cu 1 min				
80W-14Ni-6Cu 30 min				
80W-14Ni-6Fe 1 min				
80W-14Ni-6Fe 30 min				

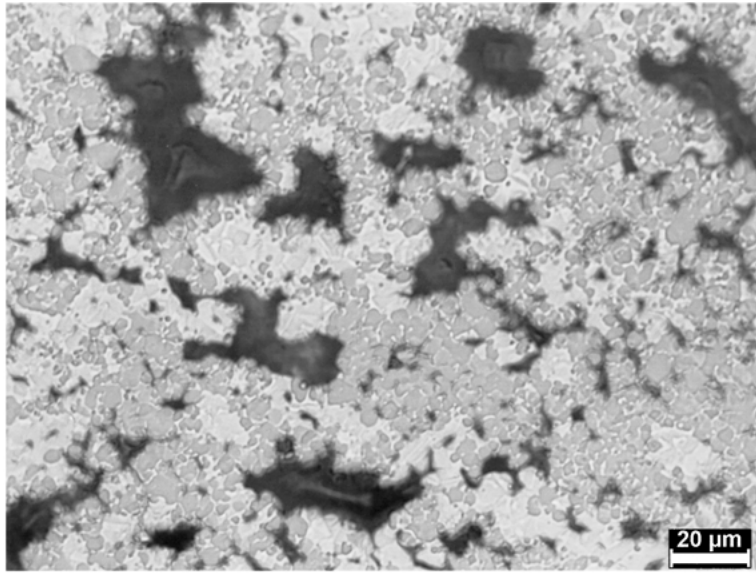
time-dependent distortion behavior observed on both compacts reflects on the deformation response of the compact as a viscous mass to the action of gravity [9]. In addition, by combining the distortion results of Table II with the density evolution shown in Fig. 3, it can be found that the density degradation after full densification results from the compact distortion.

3.5. Microstructure

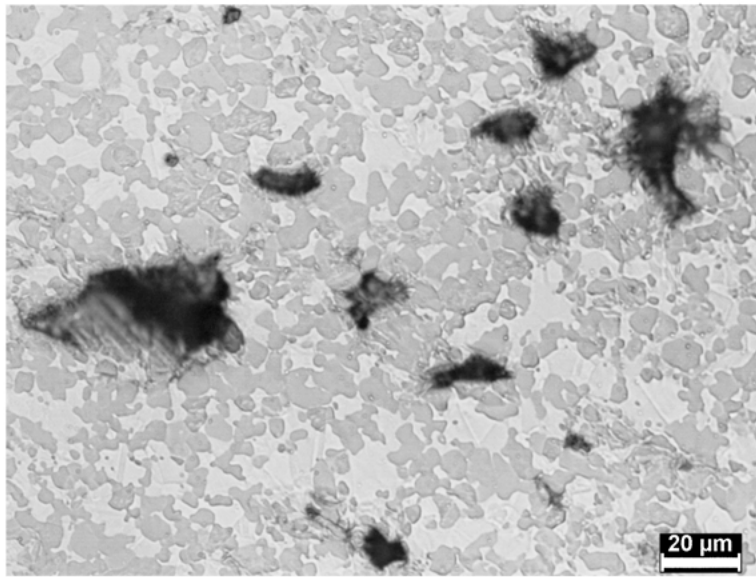
Fig. 4 shows the microstructures of the sintered 80W-14Ni-6Cu compacts without distortions. After sintering at 1275°C for 1 min (Fig. 4a), a Ni-Cu matrix (white) forms, but high porosity still exists, and the tungsten clusters have not been penetrated. Moreover, the original size and shape of the tungsten particles (gray) remain unchanged. These microstructural features indicate that liquid-phase sintering has not started at this point, thereby confirming the existence of the aforementioned LPS incubation period between 1235°C and 1287°C. When sintered to 1350°C, significant changes in the microstructure are observed (Fig. 4b). The porosity is remarkably reduced with the tungsten clusters penetrated by the liquid matrix. More important, there is obvious grain growth as well as shape accommo-

dation rounding for the tungsten grains, denoting the onset of LPS. Further increase in the sintering temperature results in a continuous decrease in porosity as well as a continuous increase in tungsten grain size (Fig. 4c). After sintering at 1450°C for 1 min (Fig. 4d), a fully dense microstructure is attained, and the tungsten grains are fairly rounded and well dispersed on the Ni-Cu matrix, which has dissolved a considerable amount of tungsten during LPS.

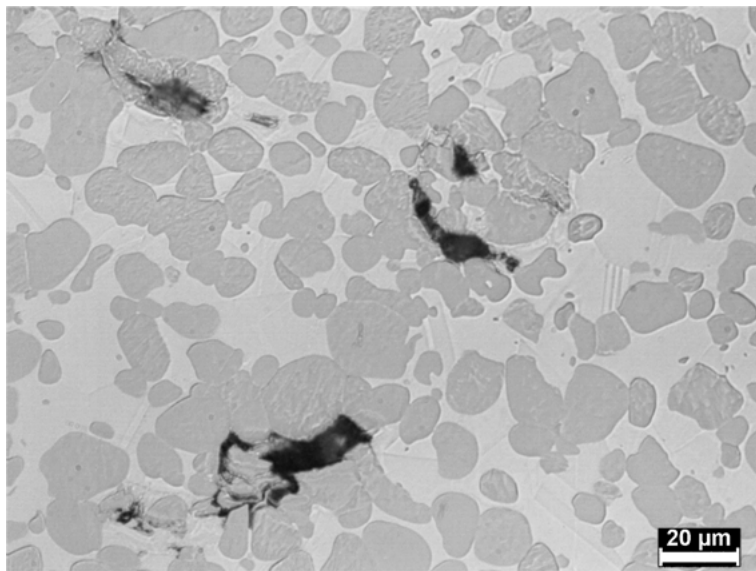
Fig. 5 shows the microstructures of the sintered 80W-14Ni-6Fe compacts without distortions. As expected, high porosity still exists after sintering at 1350°C for 1 min, and the original size and shape of the tungsten particles remain unchanged (Fig. 5a). When sintered to 1450°C (Fig. 5b) and 1475°C (Fig. 5c), the porosity is reduced continuously, with a concomitant tungsten grain growth and W-W interparticle bond growth, indicating the continued solid-state sintering in the 80W-14Ni-6Fe compact. However, once liquid-phase sintering starts, the reduction in porosity proceeds very quickly. As shown in Fig. 5d, the porosity is eliminated completely when heated to 1500°C, and the coalesced tungsten grains are penetrated and rounded into near spherical tungsten grains, with a fairly uniform distribution on the Ni-Fe-W matrix.



(a)

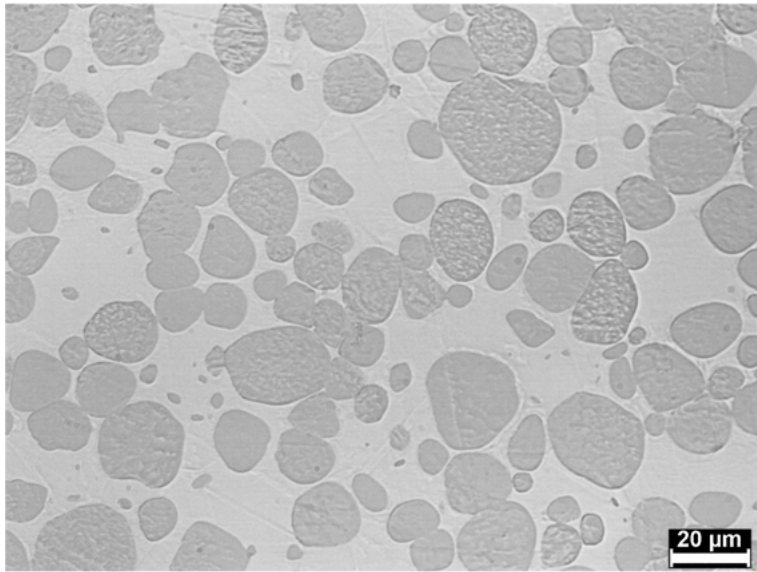


(b)



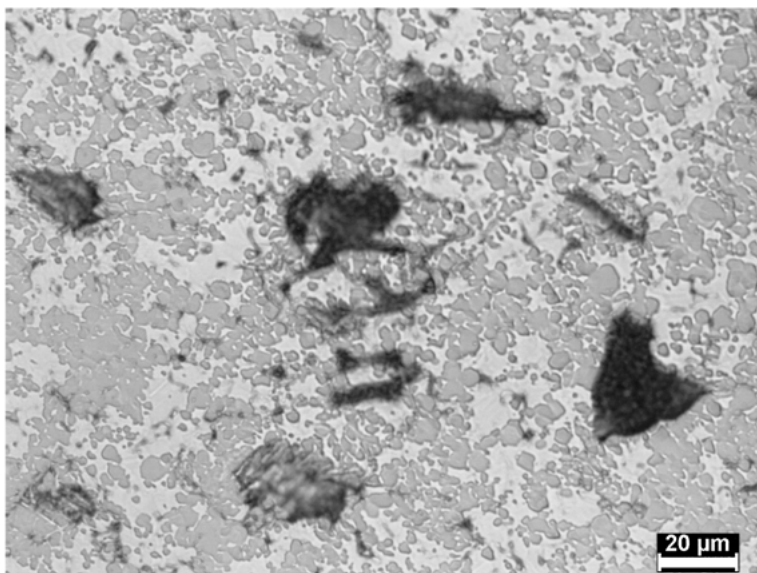
(c)

Figure 4 Microstructures of the 80W-14Ni-6Cu compacts sintered for 1 min at (a) 1275°C, (b) 1350°C, (c) 1425°C, and (d) 1450°C. (Continued)

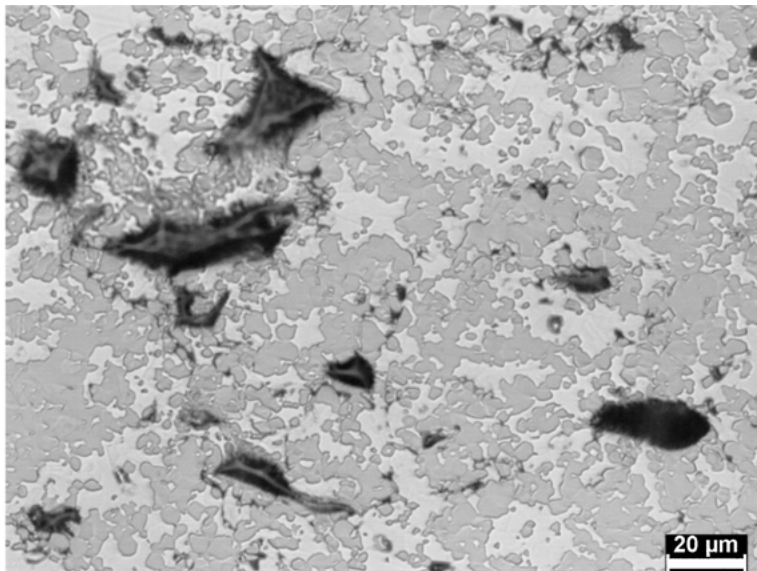


(d)

Figure 4 (Continued).

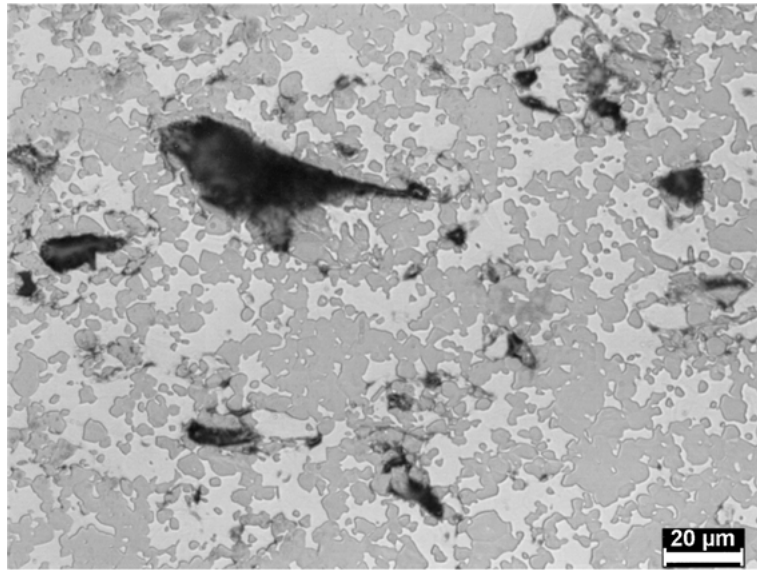


(a)

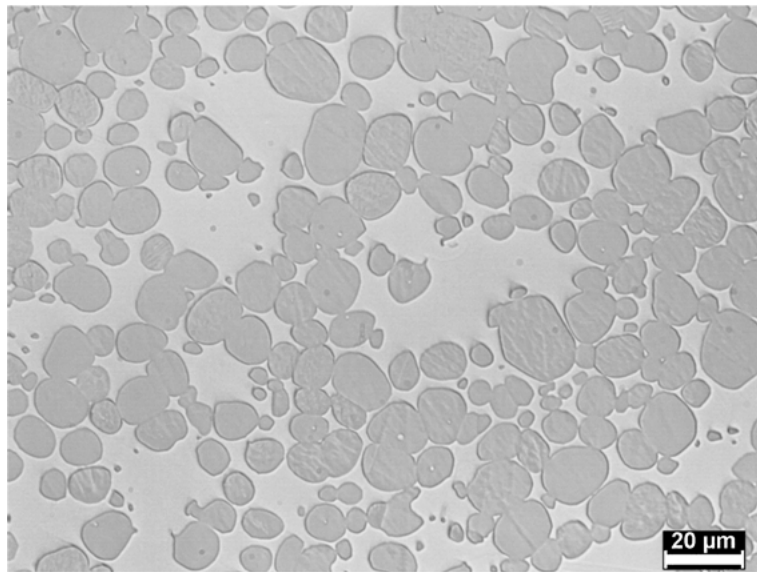


(b)

Figure 5 Microstructures of the 80W-14Ni-6Fe compacts sintered for 1 min at (a) 1350°C, (b) 1450°C, (c) 1475°C, and (d) 1500°C. (Continued)



(c)



(d)

Figure 5 (Continued).

Fig. 6 shows the microstructures of the distorted 80W-14Ni-6Cu and 80W-14Ni-6Fe compacts after sintering at 1450°C for 30 min and at 1500°C for 30 min, respectively. As can be seen, some anomalous voids with micro-crack like appearance and spherical pores are formed in these distorted compacts. Apparently, the decrease in density after full densification, as shown in Fig. 3, is caused by the development of the voids and pores upon distortion. As these voids and pores are formed after full densification of the compacts, they cannot be identified as the unfilled pores like that shown in Figs 4 and 5 [38]. Distortion is a result of loss in structural rigidity [10, 22, 27]. Hence, it can be expected that under the influence of gravity, the structurally weakened compact behaves as a fluid. In such cases, distortion is analogous to spreading of a viscous fluid. During distortion, events such as grain settling

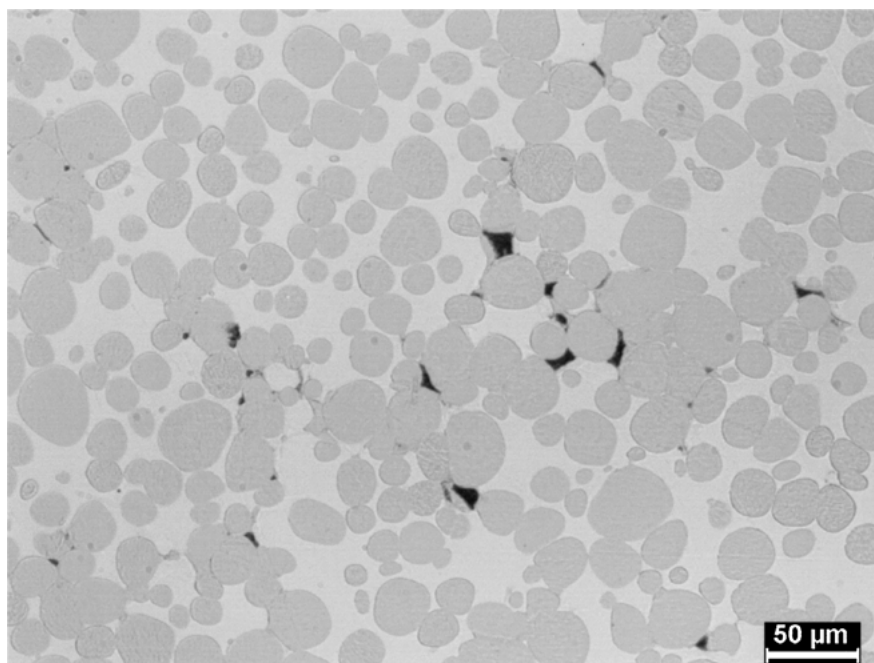
and reorientation accommodate the radial expansion. However, formation of voids along grain boundaries ensues if the rate of radial expansion exceeds that of grain settling and rearrangement.

A notable difference in the morphology and distribution of the porosity is evident from Fig. 6. The apparent reduction in the density of the W-Ni-Cu compact is dominated by the presence of crack-like voids along the grain boundaries. The pore morphology remains unaltered when sintered at 1500°C for 30 min. In the case of W-Ni-Fe, spherical pores isolated in the liquid rich area contribute to reduction in density, with a very small fraction of crack-like voids along the grain boundaries. Further, spherical pores are uniformly distributed along the entire cross section of the sintered compact (Fig. 6d) while crack-like voids are distributed in the peripheral region along the mid-height of the sample,

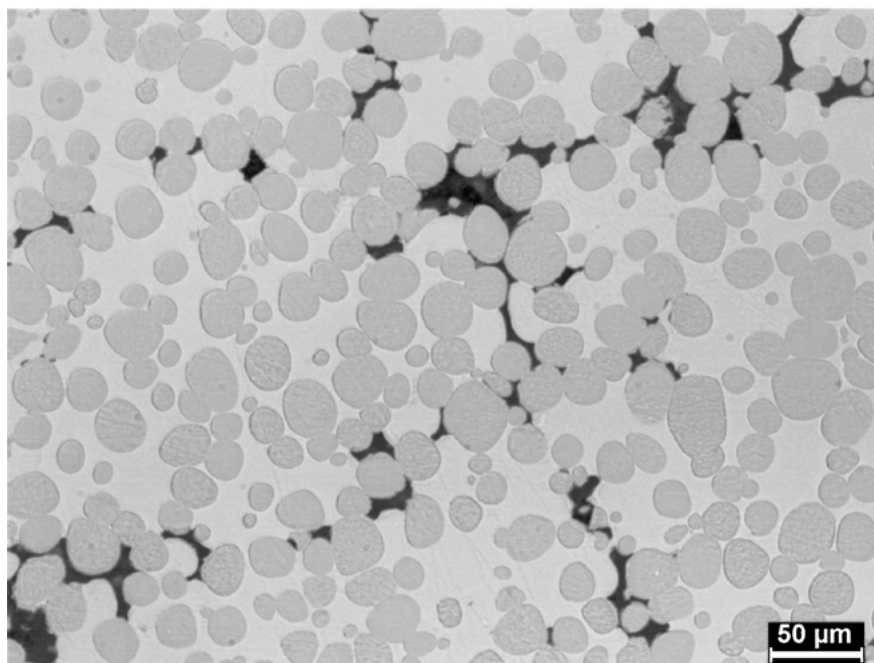
where distortion is mostly concentrated (Fig. 6b). It is likely that the difference in the void morphology is a result of different mechanisms.

Crack-like voids are formed due to compact distortion. As mentioned previously, these voids can form if the rate of radial expansion exceeds that of grain settling and rearrangement. A decrease in grain rearrangement during distortion increases the void formation. The dihedral angle, which governs the wetting and spreading characteristics of liquid phase, for the W-Ni-Fe systems

is experimentally measured to be 20° – 35° [39], while that of W-Ni-Cu is 40° – 50° [21]. Hence, it is likely that the tungsten grains are clustered with a relatively higher W-W contiguity prior to distortion in W-Ni-Cu compared to W-Ni-Fe. Further, shrinkage rate during densification indicates that dissolution of W-W contacts is slower in case of W-Ni-Cu system. Thus, grain rearrangement is impeded in W-Ni-Cu compact leading to a higher incidence of crack-like void formation during distortion compared to W-Ni-Fe compacts.

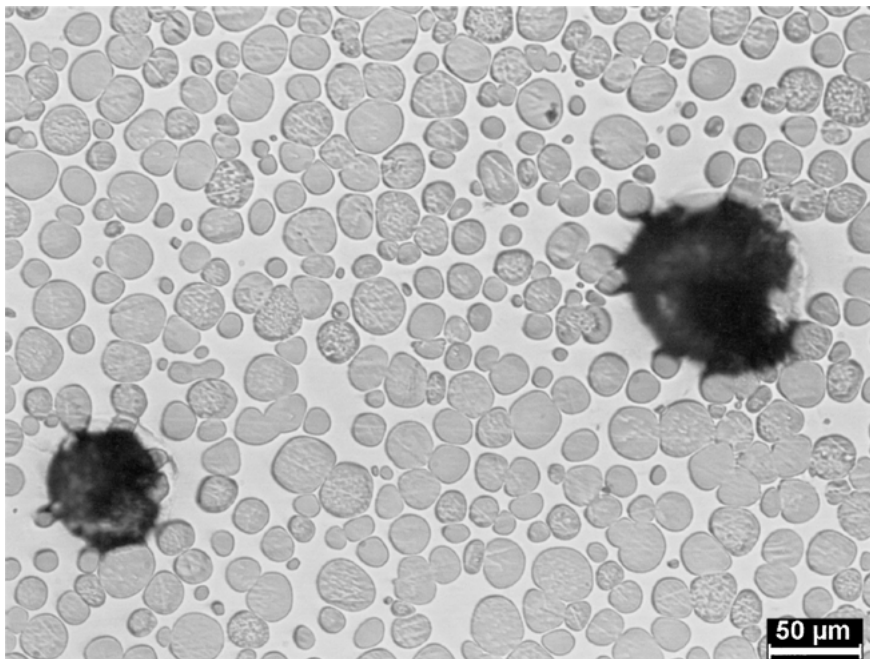


(a)

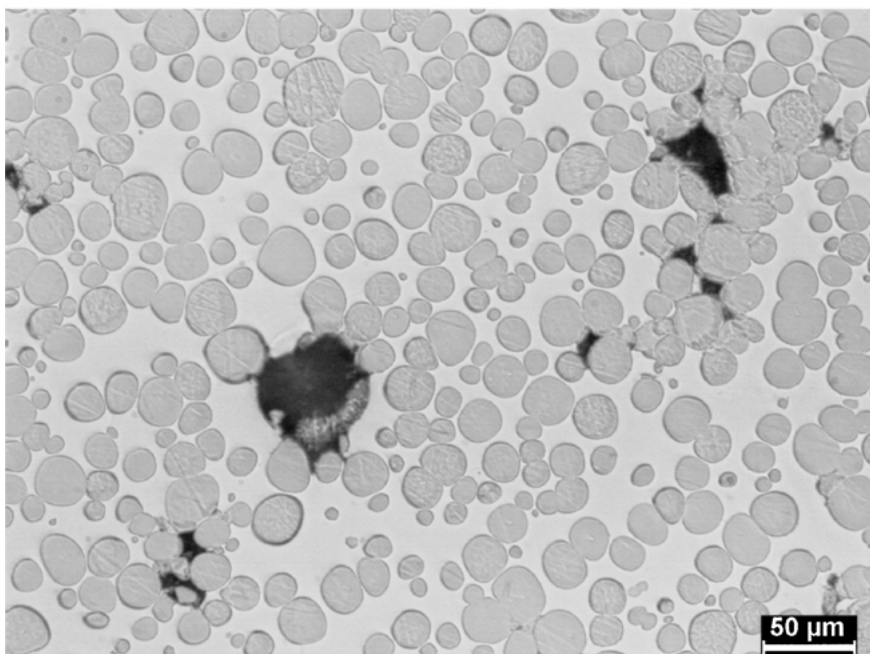


(b)

Figure 6 Microstructures of the distorted 80W-14Ni-6Cu and 80W-14Ni-6Fe compacts, after sintering at 1450°C for 30 min and at 1500°C for 30 min, respectively. (a) 80W-14Ni-6Cu, center, (b) 80W-14Ni-6Cu, mid-height peripheral region, (c) 80W-14Ni-6Fe, center, and (d) 80W-14Ni-6Fe, mid-height peripheral region. (Continued)



(c)



(d)

Figure 6 (Continued).

The spherical voids in the sintered tungsten heavy alloys are associated with the water vapor entrapment and are observed even in undistorted compacts [3, 18, 24]. The formation of water vapor is directly related to the dissolution kinetics of tungsten. During liquid phase sintering, oxygen in solution within the tungsten is released into the liquid matrix with the dissolution of tungsten grains and forms water vapor [3, 18, 24]. Since the rate of dissolution of tungsten is higher in Ni-Fe liquid phase, spherical voids are observed in W-Ni-Fe compacts and notably absent in the W-Ni-Cu compacts. It is likely that the formation of spherical voids is independent of distortion. Further efforts are

needed to explore the detailed mechanisms involved in this regard.

4. Conclusions

Inter-diffusion and *in situ* alloying take place between elemental Cu and Ni powders during solid-state heating of the W-Ni-Cu compact. As a consequence, liquid-phase sintering starts at a much lower temperature than that dictated by the phase diagram, and spans over a wide temperature range. Full densification without distortion can be achieved prior to full melting of the Ni-Cu matrix. In contrast, the melting temperature of

the Ni-Fe matrix in the W-Ni-Fe compact does not significantly change with the elemental alloying, and liquid-phase sintering proceeds dramatically within a narrow temperature range above the nickel melting point. For both alloy systems, distortion occurs if prolonging the sintering time or elevating the sintering temperature after full densification is achieved. During distortion, crack-like voids develop in the W-Ni-Cu compact due to decreased grain rearrangement, while in the W-Ni-Fe compact spherical pores are dominantly formed as a result of water vapor entrapment.

Acknowledgements

We gratefully acknowledge the funding provided by NASA for research on the Gravitational Effects on Distortion in Sintering, monitored by Michael Purvey of the Marshall Space Flight Center. Special thanks go to Louis Campbell and Kristina Cowan, P/M Lab at Penn State for their help with the DTA and dilatometry tests.

References

1. H. HOFMANN and G. PETZOW, "Modern Development in Powder Metallurgy" (Metal Powder Industries Federation, Princeton, NJ, 1985) p. 17.
2. R. M. GERMAN and K. S. CHURN, *Metall. Trans.* **15A** (1984) 747.
3. A. BOSE and R. M. GERMAN, *ibid.* **19A** (1988) 2467.
4. H. FREDRIKSSON, A. ELIASSON and L. EKBOM, *Int. J. Refract. Met. Hard Mater.* **13** (1995) 173.
5. H. RIEGGER, J. A. PASK and H. E. EXNER, "Sintering Process" (Plenum Press, NY, 1980) p. 219.
6. Y. H. CHIOU, Y. S. ZU and S. T. LIN, *Scripta Mater.* **34** (1996) 135.
7. R. M. GERMAN, S. FAROOQ and C. M. KIPPHUT, *Mater. Sci. Eng. A* **105/106** (1988) 215.
8. S. S. MANI and R. M. GERMAN, "Advances in Powder Metallurgy and Particulate Materials," Vol. 1 (Metal Powder Industries Federation, Princeton, NJ, 1990) p. 453.
9. R. M. GERMAN, "Advances in Powder Metallurgy and Particulate Materials" (Metal Powder Industries Federation, Princeton, NJ, 1999) p. 3, 139.
10. J. LIU, A. UPADHYAYA and R. M. GERMAN, *Metall. Mater. Trans.* **30A** (1999) 2209.
11. C. M. KIPPHUT, R. M. GERMAN, A. BOSE and T. KISHI, "Advances in Powder Metallurgy," Vol. 2 (Metal Powder Industries Federation, Princeton, NJ, 1989) p. 415.
12. R. M. GERMAN, *Metall. Mater. Trans.* **26A** (1995) 279.
13. Y. LIU, D. F. HEANEY and R. M. GERMAN, *Acta Metall. Mater.* **43** (1995) 1587.
14. A. UPADHYAYA, *Mater. Chem. Phys.* **67** (2001) 101.
15. B. H. RABIN and R. M. GERMAN, *Metall. Trans.* **19A** (1988) 1523.
16. B. H. RABIN, A. BOSE and R. M. GERMAN, *Int. J. Powder Metall.* **25** (1989) 21.
17. J.-K. PARK, S.-J. L. KANG, K. Y. EUN and D.N. YOON, *Metall. Trans.* **20A** (1989) 837.
18. R. M. GERMAN, A. BOSE and S. S. MANI, *ibid.* **23A** (1992) 211.
19. J. L. JOHNSON and R. M. GERMAN, *Metall. Mater. Trans.* **27B** (1996) 901.
20. J. L. JOHNSON, A. UPADHYAYA and R. M. GERMAN, "Advances in Powder Metallurgy and Particulate Materials" (Metal Powder Industries Federation, Princeton, NJ, 1995) p. 4.219.
21. A. UPADHYAYA and R. M. GERMAN, "Advances in Powder Metallurgy and Particulate Materials," Vol. 5 (Metal Powder Industries Federation, Princeton, NJ, 1996) p. 18.107.
22. *Idem.*, *Metall. Mater. Trans.* **29A** (1998) 2631.
23. J. L. JOHNSON, A. UPADHYAYA and R. M. GERMAN, *ibid.* **29B** (1998) 857.
24. X. XU, A. UPADHYAYA, R. M. GERMAN and R. G. IACOCCA, *Int. J. Refract. Met. Hard Mater.* **17** (1999) 369.
25. W. YI, X. XU, P. LU and R. M. GERMAN, *ibid.* **19** (2001) 149.
26. P. LU, R. M. GERMAN and B. MARX, *Int. J. Powder Metall.* **37** (2001) 45.
27. P. LU, X. XU, W. YI and R. M. GERMAN, *Mater. Sci. Eng. A* **318** (2001) 111.
28. S. FAROOQ, A. BOSE and R. M. GERMAN, "Progress in Powder Metallurgy," Vol. 43 (Metal Powder Association, New York, 1987) p. 65.
29. P. R. SUBRAMANIAN, D. J. CHAKRABARTI and D. E. LAUGHLIN, "Monograph Series on Alloy Phase Diagrams-10: Phase Diagrams of Binary Copper Alloys" (ASM Int., Materials Park, OH, 1994) p. 276, 475.
30. R. W. HECKEL, R. D. LANAM and R. A. TANZILLI, "Advanced Experimental Techniques in Powder Metallurgy" (Plenum Press, NY, 1970) p. 139.
31. H. BAKER, "ASM Handbook: Alloy Phase Diagrams" Vol. 3 (ASM Int., Materials Park OH, 1992) p. 2.199.
32. P. VILLARS, A. PRINCE and H. OKAMOTO, "Handbook of Ternary Alloy Phase Diagrams" (ASM Int., Materials Park, OH, 1997) p. 10670.
33. B. C. MUDDLE, *Metall. Trans.* **15A** (1984) 1089.
34. S. V. NAGENDER NAIDEN and P. RAMA RAO, "Monograph Series on Alloy Phase Diagram-7: Phase Diagrams of Binary Tungsten Alloys" (The Indian Institute of Metals, Calcutta, India, 1991) p. 89, 170.
35. A. UPADHYAYA and R. M. GERMAN, *Int. J. Powder Metall.* **34** (1998) 43.
36. V. N. ERMENKO, R. V. MINAKOVA and M. M. CHURAKOV, *Sov. Powder Metall. Metal Ceram.* **15** (1976) 283.
37. R. M. GERMAN and S. FAROOQ, "Sintering'87," Vol. 1 (Elsevier Applied Science, London, 1988) p. 459.
38. C. M. KIPPHUT, A. BOSE, S. FAROOQ and R. M. GERMAN, *Metall. Trans.* **19A** (1988) 1905.
39. S.-C. YANG, S. S. MANI and R. M. GERMAN, in "Advances in Powder Metallurgy and Particulate Materials," Vol. 1 (Metal Powder Industries Federation, Princeton, NJ, 1990) p. 469.

Received 5 June 2002

and accepted 29 January 2003